Asymmetric current collector-free interdigitated Nb_2O_5 // $LiFePO_4$ micro-batteries prepared by a simple laser-writing process

K. Brousse[1,2], P.L. Taberna[1,2] and P. Simon[1,2*]

[1] Université Paul Sabatier, Laboratoire CIRIMAT, UMR CNRS 5085, 118 route de Narbonne, 31062 Toulouse cedex 09, France

[2] Réseau sur le Stockage Electrochimique de l'Energie, FR CNRS n°3459, France

*Corresponding author.

Email : simon@chimie.ups-tlse.fr

Phone : +33 (5) 61 55 68 02

Fax : +33 (5) 61 55 61 63

Abstract

The recent development of the internet of things (IoT) raises new needs in energy storage micro-devices to power implantable and wearable applications. Conventional battery components, including electrode materials and current collectors, have to be miniaturized and integrated onto flexible substrates while keeping their electrochemical performance. Although numerous micro-fabrication processes were successfully adapted to prepare lithium-ion micro-batteries (Li-ion μbatteries), they often rely on wet processing routes such as electrochemical deposition, which does not allow the preparation of energy micro-sources at a large scale. Laser-writing processes are among the most practical and versatile methods to deposit active materials as thin films on flexible substrates. Here, we report about the integration of positive $LiFePO_4$ (LFP)-based and negative pseudocapacitive niobium pentoxide (Nb_2O_5)-based electrodes onto flexible current collector-free polyimide foils, through laser-writing of a mixture of $HAuCl_4$, cellulose acetate, and active material spray-coated films. The influence of the laser energy during the laser-writing step on the electrochemical performance of the as-prepared electrodes was studied. Laser-scribed (LS) Nb_2O_5 flexible electrodes exhibit a typical pseudocapacitive behavior, and deliver up to 114 $\mu Ah.cm^{-2}$ (205 $mF.cm^{-2}$), while 76 $\mu Ah.cm^{-2}$ were recorded for LS-$LiFePO_4$ battery electrodes prepared with the optimized laser parameters. Asymmetric Nb_2O_5 // $LiFePO_4$ micro-devices were assembled in a parallel-plate configuration, providing a 32 $\mu Ah.cm^{-2}$ areal capacity, despite the absence of any underlying current collectors. Finally, interdigitated planar asymmetric micro-batteries were realized by this simple laser-writing procedure, thus paving the path towards the facile fabrication of micro-batteries at a large scale.

Keywords: laser-writing; lithium iron phosphate; niobium oxide; micro-batteries; asymmetric devices

The continuous development of self-reliant smart wearable systems to prepare future intelligent and communicating environments called the internet of things (IoT) [1,2] brings the needs in reliable micro-sized energy storage sources such as micro-batteries (μBs) and miniaturized electrochemical capacitors (micro-supercapacitors, μSCs) [3]. Micro-supercapacitors – which store the energy via reversible et fast ion adsorption at the electrode/electrolyte interface – can deliver high peak current or power in a few seconds or ten of seconds [4,5]. Nevertheless, its low energy density limits their use to self-reliant power wearable applications. On the other hand, micro-batteries operating by faradic reactions occurring in the bulk of the electrode materials can achieve high energy densities [6]. Many battery systems were prepared at the micro-scale during the past ten years, including primary micro-batteries [7], Li-ion microbatteries [8–10], Na-ion micro-batteries [11,12], K-ion micro-batteries [13], Zn-ion microbatteries [14,15] and dual-ion microbatteries [16,17]. Pr Dunn's group reported the preparation of 3D micro-batteries based on SU-8-Coated Silicon Arrays [18]. Although the delivered capacity of 2000 $\mu Ah.cm^{-2}$ is one of the highest ever reported for a conformal all-solid-state micro-battery, on-chip fabrication processes does not allow to prepare flexible micro-batteries, which are need to power numerous wearable applications such as smart clothes, electronic papers and healthcare systems [19].

Within this scope, several designs were considered to prepare flexible microbatteries, including sandwich [20], planar interdigitated [21] or fiber-shaped [22]. One of the highest areal capacitance ever reported for a flexible Li-ion micro-battery, i.e. 5000 $\mu Ah.cm^{-2}$, was achieved with a $LiFePO_4$ (LFP) // $Li_4Ti_5O_{12}$ (LTO) asymmetric device made of micro-honeycomb graphene-CNT/active material composite electrodes [23], but the 2 mm electrode thickness does not fit with the semi-conductor industry requirements. A Li/LIBON/$LiCoO_2$ flexible encapsulated all-solid-state micro-battery was successfully prepared by a succession of layer-by-layer sputtering and thermal evaporation, and about 50 $\mu Ah.cm^{-2}.\mu m^{-1}$ were recorded [24].

However, the complex dry processing route used does not make these devices suitable for facile fabrication at a large scale.

Among the facile and scalable techniques used to prepare flexible energy storage micro-devices, printing [25–27] and laser-assisted processing [28–31] methods have attracted much interest over the past years. As an example, the screen printing of Zn // MnO_2 microbatteries supported on interdigitated graphite current collector led to high areal capacity values of 18.9 $\mu Ah.cm^{-2}$ [27]. Same procedure was applied to prepare LTO@GC||LFP@GC lithium-ion microbatteries, delivering 398 $\mu Ah.cm^{-2}$ [32]. Energy storage materials could also be embedded on flexible substrate by taking advantage of the high energy locally brought by a laser beam. Indeed, the laser insulation of polyimide or GO-based films leading to laser-induced graphene (LIG) or laser-scribed graphene (LSG), respectively, open the path towards the preparation of flexible thin-film carboneous electrode materials [33]. In this scope, photoreduced graphene was used as anode for lithium-ion systems and delivered 156 $mAh.g^{-1}$ at 40 C [30].

Another simple way to prepare microbatteries electrodes with a laser beam consists in etching the insolated active material to pattern planar micro-devices [13,34,35]. Zn nanoflakes and VO_2-MWCNTs films were prepared by vacuum filtration and laser-engraving allowed to prepare self-supported interdigitated electrodes delivering ultrahigh energy density of 188.8 $\mu Wh\ cm^{-2}$, and a high power density of 0.61 mW cm−2 [35]. Similarly, the laser patterning of electrodeposited Zn and MnO-based electrodes led to high power micro-batteries delivering 53 $\mu Ah.cm^{-2}.\mu m^{-1}$, at 1 C rate with a working voltage of 1.4 V [36]. However, the synthesis of these active materials still relies on wet processing routes which limit the preparation of such microdevices at a large scale.

The laser-ablation of casted $LiNi_{0.5}Mn_{1.5}O_4$ (LNMO) and $Li_4Ti_5O_{12}$ (LTO)-based pastes allows for preparing flexible lithium-ion microbatteries with an areal capacity of 43 $\mu Ah \cdot cm^{-2}$ at 20C [37]. Furthermore, the laser-ablation of LNMO and LTO conventional pastes was adapted to

obtain both micropillars structures and serpentine geometries [8]. The as-prepared micro-devices exhibit high areal capacities of 2500 µAh.cm^{-2} at C/10. Graphite-based dual-ion microbatteries were also prepared from the laser-ablation of doctor blade casted graphite films [16]. Once again, the preparation of such device relies on the casting of thick PVdF-based films of active material, which is not compatible with the microfabrication processes currently used in the semi-conductor industry.

An alternative approach consists in the laser-writing of the active material directly deposited on a flexible substrate. Thin-films of pseudocapacitive materials were successfully prepared by laser-scribing, which consists in insulating a composite film containing a precursor both converted in active material and adherent on the underlying substrate [38,39]. In addition, the preparation of thin-film RuO_2-based microelectrodes by a two-step laser-writing process was recently reported by our group [40]. These laser-assisted procedures provide a simple way to integrate commercial materials on flexible substrates while fitting with the common micro-fabrication requirements. However, to the best of our knowledge, laser-writing was never used to prepare lithium-ion microbatteries.

This work reports the scalable preparation of high power asymmetric $LiFePO_4$ // Nb_2O_5 micro-batteries through a simple laser-writing procedure which allows to integrate the cathodic battery material with the anodic pseudocapacitive niobium pentoxide (Nb_2O_5) onto flexible substrates to store and deliver energy.

Results

Preparation of high performance pseudocapacitive Nb_2O_5-based flexible negative electrode

The laser-writing procedure previously reported [40] was adapted to prepare Nb_2O_5-based and $LiFePO_4$-based electrodes. Here, 15 mg of active material (T-Nb_2O_5 of $LiFePO_4$) were mixed with 60 mg of a tetrachloroauric acid ($HAuCl_4.3H_2O$) gold precursor and dispersed in cellulose acetate dissolved in tetrahydrofurane (THF). The obtained ink was simply drop-casted on a flexible polyimide (Kapton^{TM}) substrate, and left under a hood to dry in air. After 5 min, laser-writing was performed on the homogeneous film to simultaneously convert $HAuCl_4.3H_2O$ into Au and induce the local sintering of the active material via the cellulose acetate pyrolysis [40]. The laser power and writing speed could be adjusted to modify the energy brought to the insolated area. Mechanically stable flexible patterned electrodes were obtained after washing in acetone and ethanol for laser beam energies ranging from 30 to 160 mJ.cm^{-1}. The nature and morphology of the as-prepared flexible electrodes were investigated by scanning electronic microscopy (SEM), X-ray diffraction (XRD) and transmission electronic microscopy (TEM). A representative SEM image of the top view of a laser-scribed $HAuCl_4.3H_2O$ – cellulose acetate / T-Nb_2O_5 electrode prepared with a laser energy of 60 mJ.cm^{-1} is shown in Figure S1A. It is seen that the current-collector-free flexible Kapton^{TM} substrate is entirely covered by the laser-scribed thin film, which is needed to provide high areal energy and power densities. In addition, the tilted view provided reveals a foam morphology inducing a rough surface with some porosity (Figure S1B), which is expected to facilitate the ion mobility during electrochemical tests. While focusing on the top of the flexible electrode prepared by this laser-writing simple procedure (Figure S1C and D), geometric grains are clearly observed. The deposit grows as small crystals with sizes ranging from 100 nm to 1 µm (Figure S1E), which is very different from the dense columnar structure related to sputtered Nb_2O_5 thin film [41], for which the deposition parameters must be carefully tuned to obtain a porous microstructure. To further investigate the morphology of the laser-scribed $HAuCl_4.3H_2O$ / T-Nb_2O_5 electrodes, and understand its composition, a focus ion beam (FIB) procedure was performed to observe the

electrode's cross-section (Figure S1F). The cross-sectional view obtained using SEM in secondary electrons mode reveals a porous structure under the FIB residual carbon protective layer, due to the large amount of grain boundaries. In order to clarify the composition of the deposit, the FIB etching procedure was performed several times and SEM images of the cross section were recorded between each step (Figure S1G and H). It appears that the deposit contains a succession of two types of grains, light and dark on the SEM image provided in **Figure 1**B, which chemical composition was investigated by EDS. In the light of **Figure 1**C, the dark grains correspond to niobium oxide, as oxygen was found in each Nb-containing grain, whereas the bright grains are made of metallic Au (no Cl atoms were found), both lying on the -C and –O containing polyimide substrate. This combination is expected to improve the electronic conductivity and charge transfer kinetics within the laser-scribed electrodes. One can note that the niobium oxide grains are still porous despite the laser-writing process used, which should provide a lot of active sites for fast redox reactions between the niobium oxide and the ion in the bulk of the electrode. Moreover, it can also be seen in Figure S1I that Au nanoparticles migrated into the polyimide substrate. This was already reported for the laser-writing of bi-layered $HAuCl_4.3H_2O$ – cellulose acetate / RuO_2 films [40], although metallic Ru was found in the first 100 nm owing to the more reductive atmosphere provided by the pyrolysis of cellulose acetate present only in the first layer.

The laser scribed $HAuCl_4.3H_2O$ / T-Nb_2O_5 electrodes were further analyzed by XRD. Figure S2A presents the XRD patterns recorded for the T-Nb_2O_5 powder (gray line) and the as-prepared electrode (green line). The peaks related to metallic Au (JCPDS 03-065-2870) are clearly visible and confirm the reduction of the gold precursor into Au, in agreement with our previous results [40] . In addition, small peaks are visible at $2\theta = 22.6°$, 28.5° and 36.8°, which were isolated on the zoom provided Figure S2B, and attributed to T-Nb_2O_5 (JCPDS 01-071-0336). The width of the peaks reveals that the as-prepared T-Nb_2O_5 has grown as small

crystallites, inducing a lot of disorder in its structure. The morphology of the as-prepared flexible electrodes was further evidenced by TEM observations (detailed in the experimental section). **Figure 1**D presents the TEM image related to a niobium oxide grain with its porosity as observed by SEM on the cross-sectional view of the electrode. The zoom on the edge of the grain provided **Figure 1**E reveals the polycrystalline structure of the T-Nb_2O_5 with small crystal sizes, with the corresponding selected area electron diffraction pattern provided in **Figure 1**F. In summary, the laser-writing of $HAuCl_4.3H_2O$ – cellulose acetate / T-Nb_2O_5 film leads to a mechanically stable porous layer made of polycrystalline T-Nb_2O_5 grains with embedded Au nanoparticles.

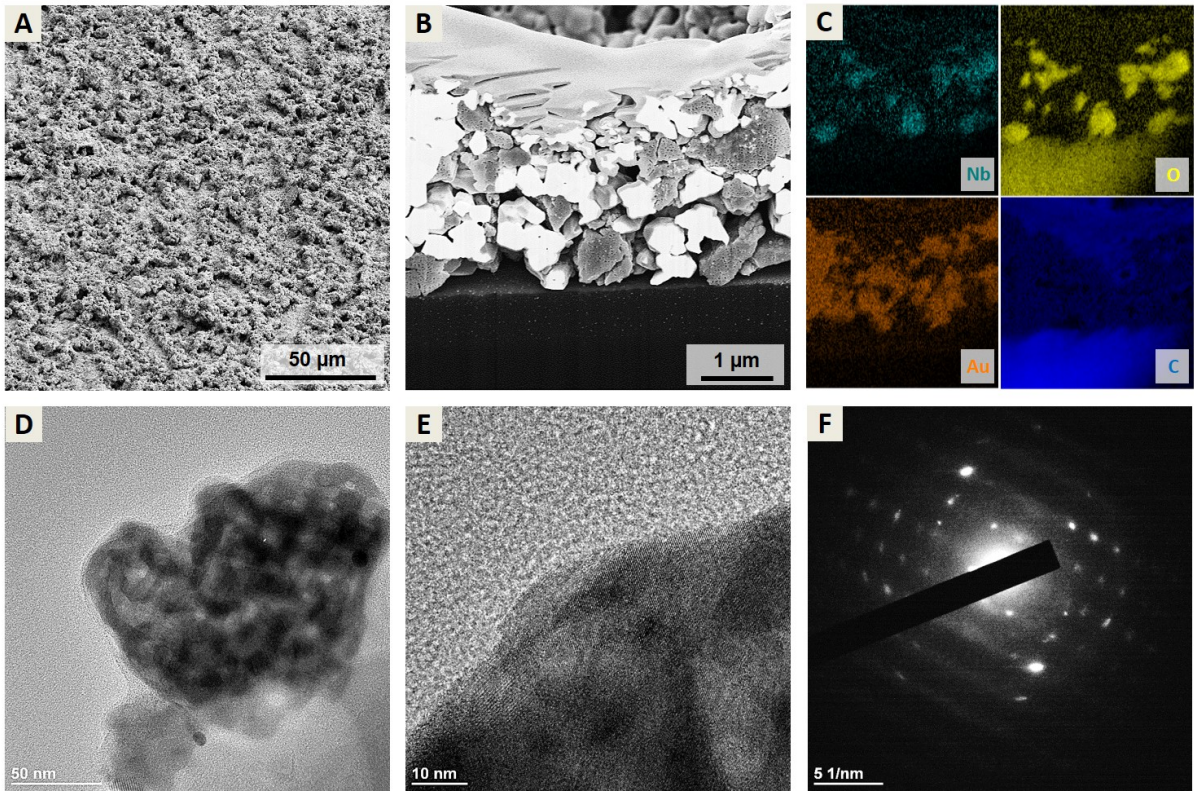

Figure 1. Nature and morphology of the laser-scribed $HAuCl_4.3H_2O$/T-Nb_2O_5 flexible electrodes. (A) Tilted image of the top (B) and cross-sectional view of the laser-scribed $HAuCl_4$/T-Nb_2O_5 with (C) the corresponding EDS map prepared via focus ion beam. (D) TEM observation of the as-prepared

electrode grains with (E) a zoom on the edge of the grain and (F) the corresponding electronic diffraction pattern.

Electrochemical characterization of the Nb_2O_5-based flexible micro-electrodes

In order to investigate the influence of the energy brought to the $HAuCl_4.3H_2O$ – cellulose acetate / T-Nb_2O_5 film during the laser-writing procedure on the electrochemical behavior of the electrodes, rectangular patterns were prepared at different laser power and writing speed. The electrodes were then assembled in a two-electrode configuration with a Li foil as both counter and reference, and further tested in a 1M lithium perchlorate concentrated propylene carbonate electrolyte (1M $LiClO_4$ + PC). T-Nb_2O_5 is expected to exhibit a pseudocapacitive behavior, which implies a fast two-dimensional Li^+ transport within the crystal structure that causes no phase changes during the electrochemical reaction [42], as described by the following mechanism (1)

$$Nb_2O_5 + xLi^+ + xe^- \Leftrightarrow Li_xNb_2O_5 \quad (1)$$

~~The cyclic voltammograms recorded at 1 $mV.s^{-1}$ for electrodes prepared from a $HAuCl_4.3H_2O$ – cellulose acetate / T-Nb_2O_5 film containing 15 mg of gold precursor (Figure S3) show an electrochemical signature characteristic of a battery-like electrode for laser energies higher than 60 $mJ.cm^{-1}$. For~~ A Au content lower than 60 mg/? leads to a pair of redox peaks corresponding to sluggish redox kinetic reactions, decreasing the power performance of the micro-devices (Figure S?). Therefore, the amount of $HAuCl_4.3H_2O$ introduced in the film before laser-writing was set at 60 mg. Aside, the rectangular patterns could be prepared using two different laser scribing orientations, i.e. vertical or horizontal, as described in Figure S4A. Indeed, the selected

direction of the laser patterning affects the length of each laser path, leading to discrepancies in heat diffusion between two laser passes, as demonstrated in previous work [40]. Thus, the direction of the laser patterning should affect the morphology of the laser-scribed Au/T-Nb_2O_5, and by extension its electrochemical response. The electrochemical behavior of two rectangular Au/T-Nb_2O_5 electrodes prepared by vertical and horizontal insulations was investigated by cyclic voltammetry. The cyclic voltammograms recorded at 5 $mV.s^{-1}$ in 1M $LiClO_4$ + PC (Figure S4B) exhibits pair of redox bumps centered at 1.8 V, typical of the pseudocapacitive signature expected for T-Nb_2O_5 [42]. Furthermore, the current (normalized to the scan rate as dQ/dE) delivered for the electrode prepared from a vertical patterning is much lower than the one delivered for the horizontal patterning, without affecting the power performance of the laser-scribed flexible electrodes. This is assumed to come from different diffusion paths of heat generated by the cellulose acetate pyrolysis under the laser beam [40], thus modifying the

sintering and adherence of the active material on the flexible substrate. This is why the rectangular electrodes prepared in this study were insulated horizontally.

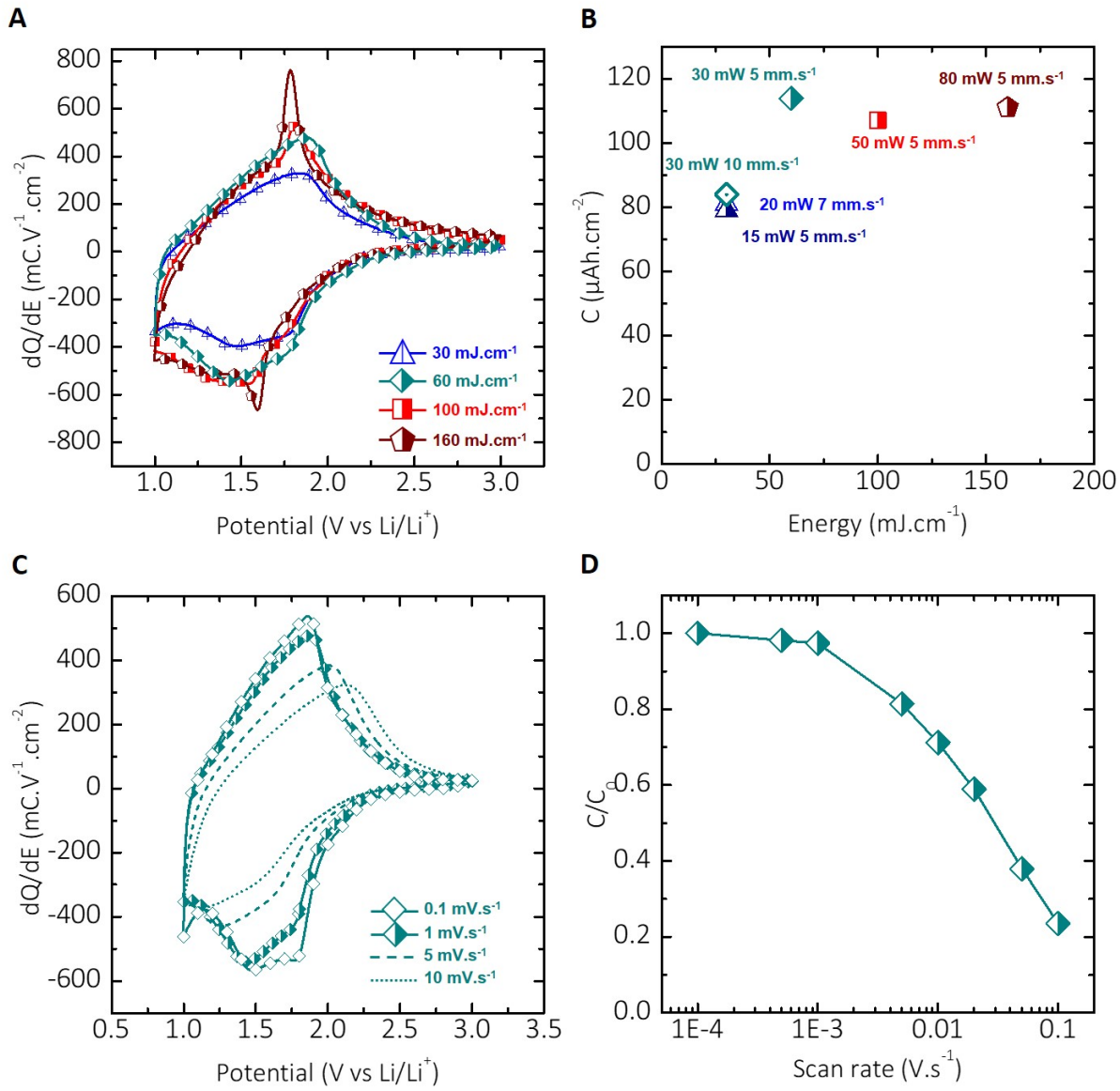

Figure 2. Electrochemical behavior of the Nb_2O_5-based flexible electrodes. (A) Cyclic voltammograms recorded at 1 $mV.s^{-1}$ in 1M $LiClO_4$ + PC for Nb_2O_5-based flexible electrodes prepared at different energies (B) with the corresponding areal capacity values. (C) Cyclic voltammograms recorded in 1M $LiClO_4$ + PC at different scan rates for a Nb_2O_5-based electrode prepared at 60 $mJ.cm^{-1}$ (D) with the corresponding change in capacitance with the scan rate.

Error! Reference source not found.A shows the cyclic voltammograms recorded in 1M $LiClO_4$ + PC at 1 $mV.s^{-1}$ for Au/Nb_2O_5 electrodes prepared from energies ranging from 30 to 160 $mJ.cm^{-1}$. The energy (integration of the laser power by writing speed) was selected as the main metrics to benchmark the electrochemical performance of the electrodes. The corresponding laser powers and writing speed are provided in Supporting Information (Figure S5A-F). The CV curves exhibit a typical pseudocapacitive shape for 30 and 60 $mJ.cm^{-1}$, with a pair of symmetrical anodic and cathodic broad peaks towards the x-axis [43]; while a pair of redox peaks appears for higher energies. In order to demonstrate the interest of this simple approach to tune the electrochemical properties of these flexible micro-electrodes, additional samples were prepared at the same energy of 30 $mJ.cm^{-1}$ (the CV corresponding to a 20 mW laser power and a 7 $mm.s^{-1}$ writing speed was also reported on Figure S5A for a matter of clarity), by adjusting the laser power and speed as shown Figure S5B and C. One electrode was prepared at a lower laser power of 15 mW by decreasing the writing speed at 5 $mm.s^{-1}$ (Figure S5B), whereas the laser power was increased at 30 mW and the writing speed adjusted at 10 $mm.s^{-1}$ for the other electrode (Figure S5C). The corresponding cyclic voltammograms recorded in 1M $LiClO_4$ + PC at 1 $mV.s^{-1}$ are very similar to the one obtained for the electrode prepared from the same energy of 30 $mJ.cm^{-1}$ (20 mW at 7 $mm.s^{-1}$), with typical pseudocapacitive signature of T-Nb_2O_5. The corresponding areal capacity values are very close to the 81 $\mu Ah.cm^{-2}$ delivered by the Au/Nb_2O_5-based electrode prepared at 20 mW for a writing speed of 7 $mm.s^{-1}$, i.e. 84 $\mu Ah.cm^{-2}$ for the laser-writing parameters 30 mW 10 $mm.s^{-1}$ and 79 $\mu Ah.cm^{-2}$ for 15 mW 5 $mm.s^{-1}$. These values were reported on **Error! Reference source not found.**B.

The highest capacity of 114 $\mu Ah.cm^{-2}$ is delivered by the electrode prepared with an energy of 60 $mJ.cm^{-1}$, (**Error! Reference source not found.**A and Figure S5D), named Au/Nb_2O_5-60, which challenges on-chip Nb_2O_5 thin films deposited by atomic layer deposition and magnetron

sputtering [41,44]. It is even close to the 146 µAh.cm^{-2} delivered by Nb_2O_5 – titanium nanotube composite electrodes supported on Ti plate [45]. Regarding the shape of the non-pseudocapacitive electrodes prepared at 100 and 160 mJ.cm^{-1} (reported also on Figure S5E and F), the Au/Nb_2O_5-60 flexible micro-electrode was tested at several scan rates to assess its power capabilities. The cyclic voltammograms recorded at 0.1 mV.s^{-1}, 1 mV.s^{-1}, 5 mV.s^{-1} and 10 mV.s^{-1} are shown in **Error! Reference source not found.**C. The current was once again normalized to the scan rate as dQ/dE, to better emphasize the curves obtained at low scan rates. The cyclic voltammograms recorded at low scan rates of 0.1 mV.s^{-1} and 1 mV.s^{-1} looks very similar to the electrochemical response of porous sputtered Nb_2O_5 [41] and Nb_2O_5 microspheres [46], exhibiting two reduction peaks located at about 1.8 and 1.5 V vs Li/Li$^+$, which were assumed to be related to the reduction of Nb^{5+} to Nb^{4+} and Nb^{+3} upon Li-ion insertion. The broad oxidation peak centered at 1.85 V vs Li/Li$^+$ suggests a continuous change from Nb^{3+} to Nb^{5+} during Li-ion deinsertion [47]. When the scan rate is increased at 5 mV.s^{-1}, the redox peaks become less visible and the potential difference between the positive and negative bumps increases owing to kinetic limitations and to the increasing ohmic drop at high current densities, which affects the capacitance retention for scan rates higher than 10 mV.s^{-1}, as reported on **Error! Reference source not found.**C. Nevertheless, the Au/Nb_2O_5 flexible electrode retains more than 50% of its initial capacitance C_0 at 20 mV.s^{-1}, and still delivers 28 µAh.cm^{-2} at a high scan rate of 100 mV.s^{-1}, corresponding to a 20 s discharge. The redox peak potential and current evolution with the scan rate were reported on Figure S6A and B, respectively. It is seen that the anodic and cathodic peak potential difference is constant (between 0.08 and 0.11 V) at low scan rates until it starts to increase at 5 mV.s^{-1} with the ohmic drop and kinetic limitations, in agreement with the previous observations regarding the cyclic voltammograms. This can be further evidenced by the change of the peak current intensity vs scan rate. Indeed, the power law in Eq. (1) is widely used to determine whether the overall electrochemical process is

diffusion controlled or not [42]. The b-exponent values is usually in the range of 0.5 to 1, if the reaction is limited by the reactive species' diffusion (b = 0.5) or not (b = 1). For the former case, it is usually assumed the charge transfer is the rate-determining step.

$$I_p = av^b \quad (1)$$

Here, the average b coefficients calculated from Eq. 1 is 0.93 for the anodic process and 0.90 for the cathodic process, which is in line with the non-diffusion limited Li^+ insertion/deinsertion process involved.

The deconvolution of the current in current contributions associated with (i) non-diffusion limited electrochemical processes and (ii) diffusion-limited electrochemical process is widely used to shed some light on the electrochemical mechanisms involved. The non-diffusion-limited contribution is considered to change linearly with the scan rate — it is defined by the k_1 coefficient —, whereas the diffusion-limited faradic reaction is considered to change with the square root of the sweep rate — it is defined by the k2 coefficient. Accordingly, the current is defined as following, Eq (2):

$$i = k_1 v + k_2 v^{1/2} \quad (2)$$

Which leads to (3) :

$$i/v^{1/2} = k_1 v^{1/2} + k_2 \quad (3)$$

When $i/v^{1/2}$ versus $v^{1/2}$ is plotted, the k_1 coefficient could be extracted from the slope of the plot, while k_2 coefficient is obtained at the y-intercept. There are two domains on the curves plotted Figure S6C, as it was already reported by Dunn's group [48]. The current is proportional to the scan rate before 10 $mV.s^{-1}$, where the electrode behaves as a thin layer, which results in a reversible lithiation and delithiation in the whole bulk. In this region, k_1 = 90 $mAs.V^{-1}$ and k_2

is lower than 0.1 $mAs^{1/2}V^{-1/2}$ for the anodic process, (-72 $mAs.V^{-1}$ and -0.6 $mAs^{1/2}V^{-1/2}$ for the cathodic one). For higher scan rates, solid diffusion limitations appears and the k_2 coefficient becomes non-negligeable (k_1 = 31 $mAs.V^{-1}$ and k_2 = 4 $mAs^{1/2}V^{-1/2}$ for the anodic process, -38 $mAs.V^{-1}$ and -3 $mAs^{1/2}V^{-1/2}$ for the cathodic one). These observations confirm the pseudocapacitive behavior of the as-prepared Au/Nb_2O_5 electrodes.

Preparation of a battery-like $LiFePO_4$-based flexible positive electrode

Same process was applied to integrate $LiFePO_4$ onto polyimide substrates. The amount of active material and $HAuCl_4.3H_2O$ were kept at 15 mg and 60 mg, respectively. The laser-writing energy was set at 60 $mJ.cm^{-1}$ (30 mW and 5 $mm.s^{-1}$). After laser-writing and washing with acetone and ethanol, laser-scribed $HAuCl_4.3H_2O$ – cellulose acetate / $LiFePO_4$ electrodes were characterized by SEM and TEM. As for the Au/Nb_2O_5 electrodes, it is seen, on the tilted view of the electrode surface shown **Figure 3**A, that the rough deposit covers the polyimide surface. The zoom in Figure S7A allows to observe the porous foam obtained after laser-writing, with sub-micron sized spherical particles (balls) on the top. The observation of the electrode cross-section prepared by FIB (**Figure 3**B) reveals that the deposit grew as a bush-like structure, with sub-micrometer large balls embedded in the porosity as shown **Figure 3**C. One can notice the absence of geometric grains while comparing to the structure of the Au/Nb_2O_5 electrodes, which suggests different growing mechanisms owing to the difference in laser absorbance and thermal conductivity of these two different active materials [33]. Aside, the laser-writing of $HAuCl_4.3H_2O$ – cellulose acetate / $LiFePO_4$ films did not lead to the migration of Au nanoparticles (see Figure S7B) in the polyimide as it was the case for the Au/Nb_2O_5 flexible electrodes. EDS mapping of the deposit (Figure S7C-F) demonstrates that $LiFePO_4$ – evidenced by XRD as shown Figure S8, JCPDS 00-040-4099 – is found in the bulk of the electrode, while

sub-micrometer Au balls migrated into the porosity. This was further confirmed by TEM. **Figure 3**D presents the TEM observation of the Au/$LiFePO_4$ bushes, where the Au particles appears in dark contrast. The bulk of the grains contains highly ordered planes (**Figure 3**E), as confirmed by the SAED pattern (**Figure 3**F), with amorphous structures on the edges. Thus, the laser-writing of $HAuCl_4.3H_2O$ – cellulose acetate / $LiFePO_4$ leads to an adherent deposit with $LiFePO_4$ bushes-like structure and Au particles embedded.

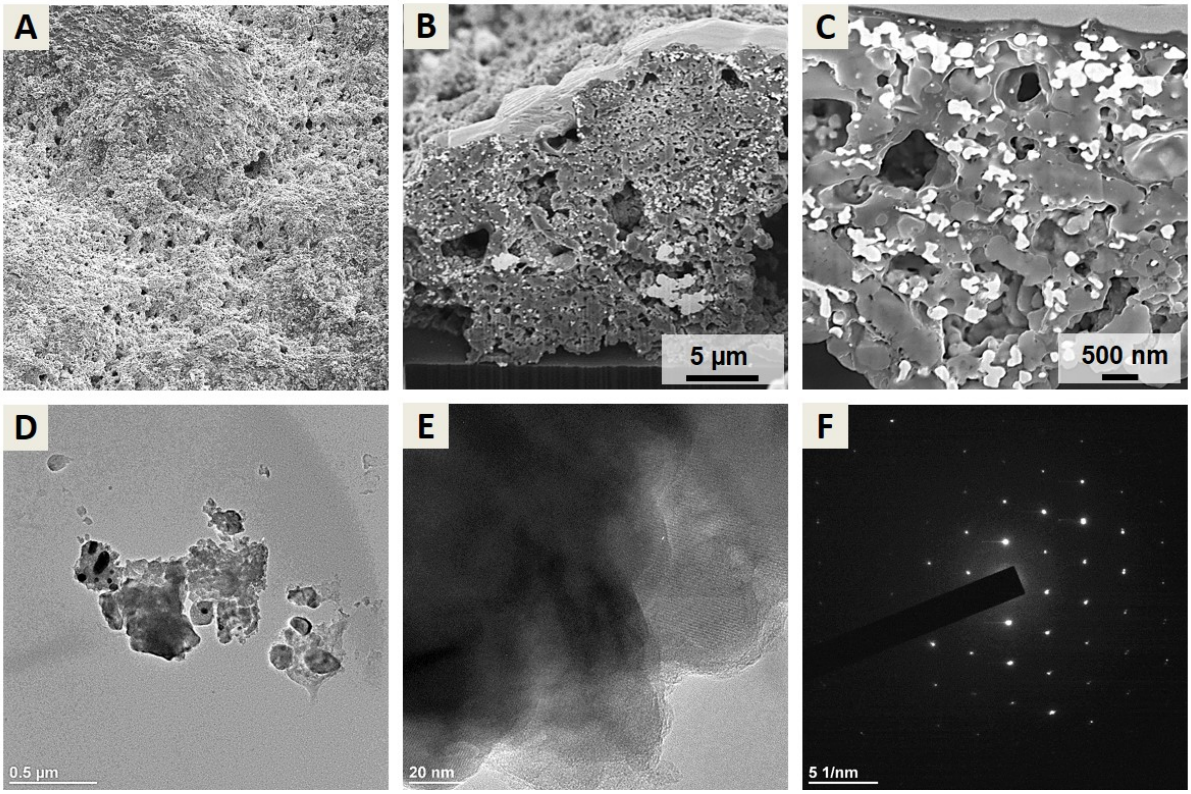

Figure 3. Nature and morphology of the flexible electrodes prepared by laser-writing of carbon-coated $LiFePO_4$. (A) SEM images in SE mode of the top (tilted view) and (B) cross section of the electrode prepared by focused ion beam (C) with the corresponding zoom. (D) TEM image of laser-scribed Au/$LiFePO_4$ grains (E) with the corresponding high resolution TEM image and (F) selected area electron diffraction pattern.

Electrochemical characterization of the battery-like $LiFePO_4$-based flexible electrode

The laser-writing parameters were adjusted to prepare Au/$LiFePO_4$ current-collector-free flexible electrodes at different laser energies, and their electrochemical behavior was investigated by cyclic voltammetry in 1M $LiPF_6$ dissolved in EC:DMC (1:1), also known as LP30. **Figure 4**A presents the cyclic voltammograms recorded at 1 $mV.s^{-1}$ in LP30 electrolyte. CVs exhibit the expected pair of redox peaks for a LFP electrode, corresponding to the oxidation (positive current), standing for the extraction of Li^+ ions from the LFP, and the reduction (negative current) of the material upon cycling through Li^+ insertion in the delithiated $FePO_4$ phase [49]. For a beam energy of 30 $mJ.cm^{-1}$, broad oxidation and reduction peaks are visible, while they thin out when the energy increases to 60 $mJ.cm^{-1}$, delivering 235 $mC.cm^{-2}$ during the reduction process, i. e. 65 $\mu Ah.cm^{-2}$. Then, the peaks intensity decreases drastically when the energy reaches 80 $mJ.cm^{-1}$ and becomes negligible for 120 $mJ.cm^{-1}$. Therefore, the electrode prepared at 60 $mJ.cm^{-1}$ (Au/$LiFePO_4$-60) was cycled at different scan rates to assess its electrochemical performance. The corresponding CVs presented **Figure 4**B are normalized to the scan rate as $mAs.V^{-1}cm^{-2}$ to make the curves corresponding to the small scan rates visible. The cyclic voltammogram recorded at 0.1 $mV.s^{-1}$ shows the oxidation and reduction peaks expected for electrochemically active LFP, centered at 3.4 V vs Li/Li^+. The areal capacity calculated from the reduction peak is 76 $\mu Ah.cm^{-1}$ as it can be seen **Figure 4**C. This challenges LNMO micro-electrodes prepared by magnetron sputtering, which deliver 22.5 $\mu Ah.cm^{-2}$ [50]. When the scan rate is increased of one order of magnitude, the redox peaks tend to broaden while the peak separation slightly increases as evidenced from the slope of the ΔE vs scan rate curve (**Figure 4**D, inset). This is due to the redox reactions involved in the charge storage mechanism in comparison with the Au/Nb_2O_5 electrode. When the scan rate reaches 5 $mV.s^{-1}$, a distortion of the CV curves appears due to ohmic losses, and the peak separation starts to increase drastically. Still, the Au/LFP current-collector-free flexible electrode delivers 30 $\mu Ah.cm^{-2}$ at 20 $mV.s^{-1}$, thus demonstrating that the as-prepared electrodes are suitable for high

power demand. The mean potential, calculated from the difference between anodic and cathodic peak potentials, was also reported on **Figure 4**D, showing that it is kept constant at 3.43 V vs Li/Li^+ on the whole range of sweep rates. The peak shift magnitude is thus the same for both charge and discharge processes. The electrochemical behavior of the Au/LFP micro-electrodes could be further investigated by plotting the change of the peak current i_P versus the scan rate ν in a logarithm scale as in **Figure 4**E. Despite a slight change of the slope observed for scan rates higher than 5 $mV.s^{-1}$, the average b coefficients calculated from Eq. 1 is 0.56 for the anodic process and 0.55 for the cathodic process, which is in line with an overall electrochemical process controlled by the diffusion, while occurs Li^+ insertion/deinsertion.

Figure 4F shows the change of the anodic and cathodic peak intensities with the sweep rate according to Eq (3). The sudden change of slope observed before 5 $mV.s^{-1}$ suggest that the charge storage process follows several electrochemical behaviors depending on the scan rate, and the plot can be split into two zones. At low scan rates (< 5 $mV.s^{-1}$), k_1 = 99 $mAs.V^{-1}$ and k_2 = 6 $mAs^{1/2}V^{-1/2}$ for the anodic process, (-59 $mAs.V^{-1}$ and -6 $mAs^{1/2}V^{-1/2}$ for the cathodic one), which means that the current is proportional to the scan rate instead of its square root. Thus, the charge storage mechanism is not limited by the Li^+ diffusion before 5 $mV.s^{-1}$, and the electrode behaves like a thin-layer, in which the lithiation/delithiation occurs in the whole bulk. It was already observed by Come et al. for $LiFePO_4$ tested in a cavity microelectrode [49]. For higher scan rates, the k_1 value is negligible compared to k_2 (k_1 = 0.2 $mAs.V^{-1}$ and k_2 = 9 $mAs^{1/2}V^{-1/2}$ for the anodic process, -2 $mAs.V^{-1}$ and -8 $mAs^{1/2}V^{-1/2}$ for the cathodic one), which suggests that the reaction becomes limited by the Li^+ solid diffusion.

These performances make the as-prepared $Au/LiFePO_4$ electrodes suitable as positive electrode in asymmetric micro-devices which could handle high power demand.

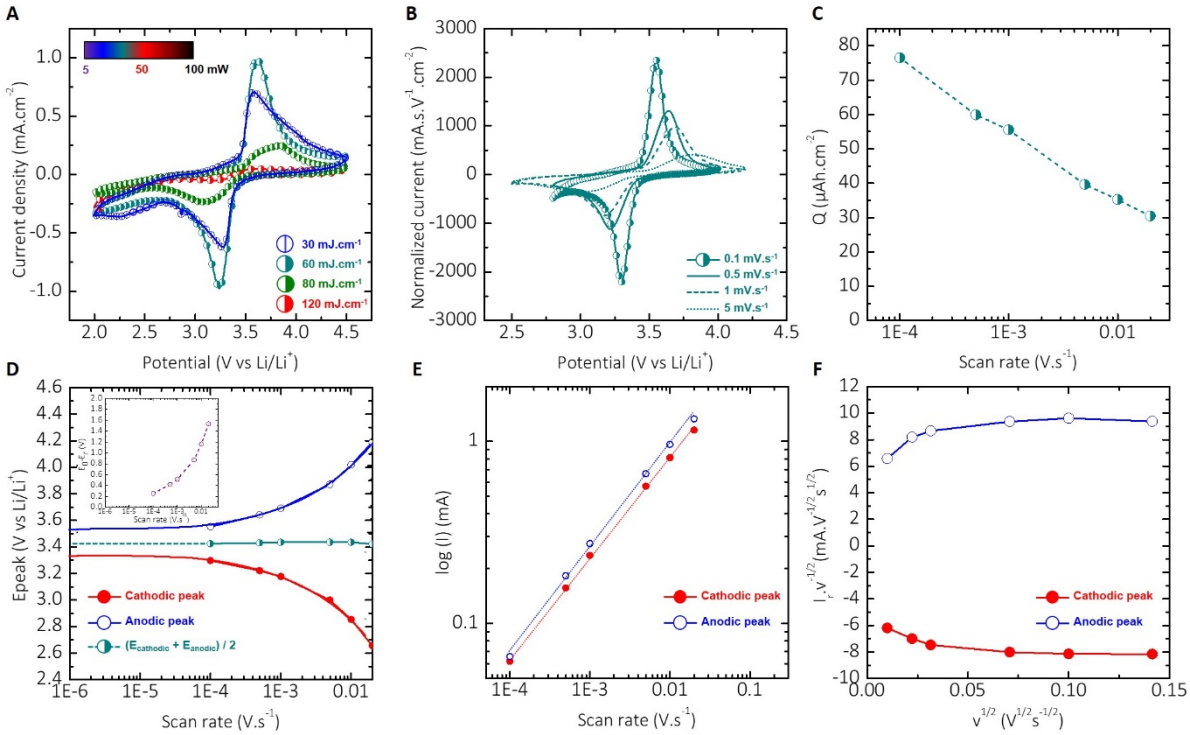

Figure 4. Electrochemical behavior of the $LiFePO_4$-based flexible electrodes. (A) Cyclic voltammograms recorded at 1 $mV.s^{-1}$ in 1M $LiPF_6$ + EC:DMC (1:1) for $LiFePO_4$-based flexible electrodes prepared at different laser powers and writing speeds. (B) Cyclic voltammograms recorded in LP30 at different scan rates for a $LiFePO_4$-based electrode prepared at 60 $mJ.cm^{-1}$ (30 mW and 5 $mm.s^{-1}$) (C) with the corresponding change in capacity with the scan rate. (D) Change of the redox peaks potential and (E) current. (F) Deconvolution of the non-diffusion-limited and diffusion limited current contributions.

Asymmetric Nb_2O_5 // $LiFePO_4$ micro-batteries

This simple fabrication process was used to prepare asymmetric Nb_2O_5 // $LiFePO_4$ flexible micro-batteries. In order to assess the electrochemical performance of such micro-device while getting rid of the limitation related to the device geometry (planar or interdigitated electrodes, length of the gap between the electrodes), a positive Au/$LiFePO_4$-60 electrode and a negative Au/Nb_2O_5-30 electrode – of which the areal capacity close to the Au/$LiFePO_4$ capacity allows to equilibrate the system – were immersed in a 1M $LiClO_4$ + PC electrolyte in a parallel-plate configuration, and a Li foil was added as reference electrode to record the change of potential of both electrode during cycling. Prior to galvanostatic charge-discharge tests, cyclic

voltammetry was performed several times to reach a stabilized electrochemical response. Then, the potential of the $LiFePO_4$–based electrode was held at 3.35 V vs Li/Li^+ for 20 min, and the potential of the Nb_2O_5-based electrode was held at 3.05 V vs Li/Li^+ for 20 min to keep the full device to its discharge state. Then, GCPL was performed on the asymmetric Nb_2O_5 // $LiFePO_4$ cell and the voltage window was controlled between 0.3 V and 2.5 V to keep each electrode in its operating potential range. **Figure 5**A presents the charge and discharge curves recorded at 0.5C. During the cell charge (blue dashes related to the right axis), the cell voltage increases from 0.3 V to 2.5 V, exhibiting a plateau at an average voltage of 1.75 V with a slight slope owing to the electrochemical kinetics of the redox reactions occurring at the Nb_2O_5-based pseudocapacitive electrode [48]. Indeed, while looking at the potential of each electrode separately (red and green symbols related to the left axis), it is observed a plateau at 3.45 V vs Li/Li^+ corresponding to the delithiation process occurring at the LFP electrode, which ends at the working potential limit of 3.8 V vs Li/Li^+. Meanwhile, the potential of the Nb_2O_5-based electrode first decreases from 3.05 V vs Li/Li^+ to 2.0 V vs Li/Li^+, where the intercalation reaction starts, before a linear decrease is observed until 1.3 V vs Li/Li^+, which is the expected potential window for pseudocapacitive Nb_2O_5. During the cell discharge, the potential of the LFP electrode decreases and exhibits a plateau at 3.35 V vs Li/Li^+ corresponding to the lithiation process. At the Nb_2O_5-based electrode, the potential increases linearly from 1.3 V vs Li/Li^+ to 3.05 V vs Li/Li^+, thus inducing a discharge plateau at 1.5 V on the full cell discharge curve.

GCPL was performed at C rates ranging from 0.5C to 10C, and the recorded charge-discharge curves are presented **Figure 5**B. Once again, a discharge plateau is observed at an average voltage of 1.5 V. The discharge capacity delivered by the micro-device at 0.5C reaches 32 $\mu Ah.cm^{-2}$. Thus, this simple laser-writing process provides an easy way to prepare asymmetric Nb_2O_5 // $LiFePO_4$ micro-batteries delivering areal capacity in the same order of magnitude that Zn // MnO_2 or Li-ion microbatteries prepared from multistep electrodeposition routes (50-80

$\mu Ah.cm^{-2}.\mu m^{-1}$) which does not fit the semi-conductor industry requirements [36][51]. Also, the areal capacity may be increased by scribing thicker deposit. When the C-rate increases, the capacity delivered decreases due to the diffusion limitations occurring at the $LiFePO_4$ electrode, while the Nb_2O_5-based electrode becomes overcapacitive at such small discharge time. Nevertheless, the micro-device still retains almost 40% of the initial capacity at 10 C as shown **Figure 5**C, which makes asymmetric Nb_2O_5 // $LiFePO_4$ flexible electrodes suitable for high power energy supply.

Miniaturized energy-storage devices are needed to power portable electronic devices and applications, such as RFID tags for example. Therefore, the volume of the energy sources has to be minimized, and micro energy storage devices are often patterned as planar interdigitated electrodes. In this work, the simple laser-writing process used not only allows to get rid of the complex lithography and etching processes implied for the deposition and patterning of current collectors and active material, but also to easily tune the electrodes geometry. As direct evidence, asymmetric interdigitated Nb_2O_5 // $LiFePO_4$ micro-batteries were prepared. Briefly, an Au/Nb_2O_5 negative electrode was first deposited and patterned as interdigitated fingers through the laser-writing of a $HAuCl_4.3H_2O$ – cellulose acetate / T-Nb_2O_5 film drop-casted on the flexible polyimide substrate (the beam energy was 30 $mJ.cm^{-1}$). The deposit was further washed with acetone and ethanol, and a new $HAuCl_4.3H_2O$ – cellulose acetate / $LiFePO_4$ film was used to cover on the whole polyamide substrate. A second laser-writing step (60 $mJ.cm^{-1}$) was performed in order to deposit and pattern a positive Au/$LiFePO_4$ electrode as interdigitated fingers. The interspace between the positive and negative electrodes was set at 300 µm to avoid any short circuits. A thin protective Au layer was deposited on the edge of the device in order to prevent any electrode alteration by the tweezers used for electrochemical tests. The as-prepared flexible micro-battery (inset of **Figure 5**D) was immersed in the 1M $LiClO_4$ + PC electrolyte, and tested by GCPL. After a first charge-discharge was performed at 1C, GCPL

measurements were performed three times at C-rates ranging from 1 C to 50 C, as reported on **Figure 5**D. The interdigitated micro-battery delivers more than 10 µAh.cm^{-2} at 1 C, as shown by the corresponding charge and discharge curves plotted on **Figure 5**E. The loss of areal capacity compared to Nb_2O_5 // $LiFePO_4$ assembled in parallel plate is due to the planar configuration in which the areal capacitance is twice lower than for a sandwich configuration. In addition, some electrochemically active sites are blocked by the Au protective layer, thus reducing the amount of charge stored in the micro-electrodes. The micro-battery still delivers 7 µAh.cm^{-2} at 50 C, i. e. 58% of the initial capacity, which is in agreement with the interesting power capabilities obtained in parallel-plate configuration. In order to assess the cyclability of the micro-devices, same interdigitated Nb_2O_5 // $LiFePO_4$ micro-batteries were prepared, and galvanostatic charge-discharge tests were performed in 1M $LiClO_4$ + PC at 10 C over 1000 cycles. The discharge capacity values recorded are reported on **Figure 5**F. The asymmetric interdigitated Nb_2O_5 // $LiFePO_4$ micro-battery retains 80% of its initial capacity after 1000 cycles. The 20% capacity loss during the first 100 cycles are attributed to the stabilization of the electrodes faradic efficiencies through progressive formation of solid electrolyte interface (SEI). These performance makes interdigitated flexible Nb_2O_5 // $LiFePO_4$ asymmetric micro-batteries promising to deliver decent energy densities within short times.

Performance-wise, the herein devices are not as good as those of the literature, but they shine concerning the effectiveness of the fabrication process: in one-pot electrode synthesis and elaboration are achieved and it is extendable to a wide variety of active materials. As results, it is cost effective, so easily upscalable.

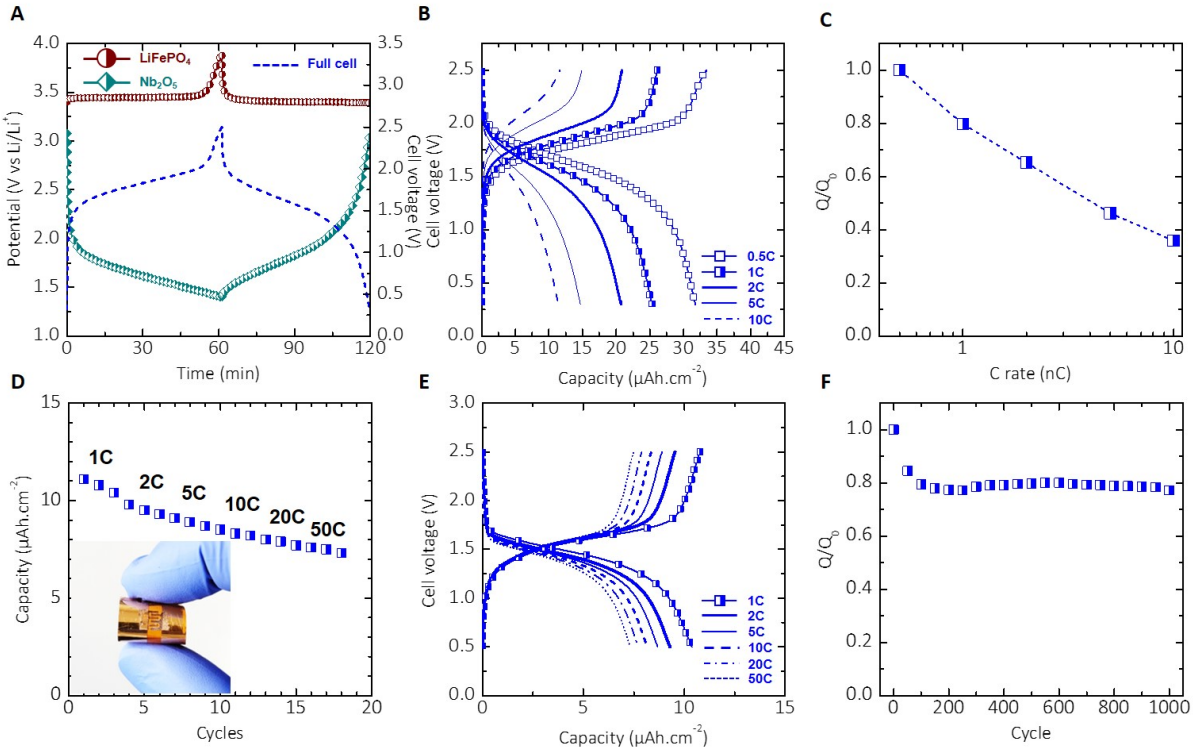

Figure 5. Electrochemical behavior of flexible Nb_2O_5 // $LiFePO_4$ asymmetric devices. (A) Charge-discharge curves recorded at 0.5C for an asymmetric Nb_2O_5 // $LiFePO_4$ micro-battery tested in a parallel-plate configuration in 1M $LiPF_6$ + EC:DMC (1:1). (B) Charge-discharge curves recorded at different C rates (C) with the corresponding change in capacity with the C rate. (D) Areal capacity values recorded for an interdigitated micro-device (inset) at different C rates with (E) the corresponding galvanostatic charge discharge curves. (F) Cyclability test performed at 10C over 1000 cycles.

Conclusion

For the first time, a simple laser-writing process allowed to prepare flexible $LiFePO_4$ and Nb_2O_5-based electrodes onto raw, current collector-free polyimide film. The laser writing of $HAuCl_4.3H_2O$ – cellulose acetate – Nb_2O_5 films lead to a porous Au-Nb_2O_5 porous deposit adhering to the polyimide. The energy brought to the film during the laser-writing process plays a role on the Au/Nb_2O_5 current-collector-free electrodes electrochemical behavior, and a high areal capacitance values up to 114 µAh.cm^{-2} (205 mF.cm^{-2}) for an optimized energy of 60 mJ.cm^{-1}. Faradic Au/$LiFePO_4$ flexible electrodes were also prepared, and delivered decent areal capacities up to 76 µAh.cm^{-2} despite the absence of current collector underneath. The positive

and negative electrodes were used together in a parallel-plate configuration to build an asymmetric Nb_2O_5 // $LiFePO_4$ micro-battery. The as-prepared micro-device exhibited a discharge plateau with a slight slope at 1.5 V owing to the different kinetic mechanisms involved at the faradic and pseudocapacitive electrodes. The device discharge capacity reached 32 $\mu Ah.cm^{-2}$ at 0.5 C, and the micro-battery still retained 40% of the initial capacity at 10 C. As a proof of concept, planar interdigitated Nb_2O_5 // $LiFePO_4$ asymmetric micro-batteries were successfully prepared onto current-collector-free polyimide, and retained 80% of the areal capacity after 1000 cycles, thus making this laser-writing process promising for the facile and scalable fabrication of flexible micro-batteries at a large scale.

Methods

Materials. Chloroauric acid ($HAuCl_4.3H_2O$), Tetrahydrofuran (TFH) and cellulose acetate were purchased from Sigma Aldrich, while Kapton foil (50 µm-thick) was obtained from RS components. A DILASE 250 UV laser (405 nm, KLOÉ, France) was used with the software KloeDesign. The energy brought to the system during insolation was tuned by adjusting the laser power and writing speed. The maximum output power was measured at 285 mW, the writing speed varies from 0.1 and 10 $mm.s^{-1}$ with a 5 µm spot size.

Electrode preparation. A Polyimide (PI) film was chosen for its thermal stability and low surface roughness. A Ti/Au current collector could be sputtered on the PI foil to provide a good electronic conduction during electrochemical characterizations. Then, 500 mg of cellulose acetate were dissolved in 20 mL of tetrahydrofuran (THF) under stirring for 1h. Subsequently, 60 mg of $HAuCl_4.3H_2O$ and 15 mg of active material were mixed and added in 0.5 mL of the cellulose acetate/THF solution. The $HAuCl_4.3H_2O$ – cellulose acetate – active material dispersion was drop-casted on the current-collector-free flexible substrate. Finally, the

electrodes were patterned by performing laser-writing of the homogeneous film. The areas that were not irradiated by the laser were easily removed by washing with acetone and ethanol aliquots. Several laser power and writing speed were used to study the influence of the insulation energy on the electrochemical behavior and performance of the laser-scribed electrodes.

Characterizations. X-Ray diffraction (XRD) patterns of the deposits were recorded by a D4 ENDEAVOR diffractometer (Brucker, Germany) using a Cu Kα radiation (λ = 0.154 nm) from 2θ = 20° to 2θ = 80°.

The structure of the laser-scribed RuO_2 was observed through Scanning Electron Microscopy (SEM) with a JSM 7100F (JEOL, Japan) with an acceleration voltage of 15.0 kV. The EDS maps have been analyzed using the AztecONE software by Oxford Insruments.

The TEM images were obtained using a probe corrected cold-FEG JEM-ARM200F (JEOL, Japan) operated at 200 kV, equipped with an energy dispersive X-ray spectrometer (EDS). The flexible electrodes were hardly scratched with a ceramic spatula to obtain a powder. The material was sonicated for 10 min before drop-casting on the TEM grid.

The cross-specimen used for SEM observations has been obtained using a MEB/FIB FEI HELIOS 600i equipped with a gas injection system and an EDX detector.

The electrochemical characterizations of the as-prepared electrodes were carried out using a Biologic VMP3 Potentiostat in 1M $LiClO_4$ + PC with a Li foil as both counter and reference in a two-electrode configuration. The asymmetric devices in parallel-plate and planar interdigitated configurations were tested in two-electrode configuration, by taking the electrical contacts on an Au protective layer sputtered on the edge of each interdigitated electrode.

Acknowledgements

We acknowledge support from the Chair of Excellence from the Airbus Group and ANR Labex Store Ex program. We are grateful to CNRS, INSA and Université Paul Sabatier (Toulouse III) for their support. We thank C. Josse for SEM observations and cross-section preparation, and S. Duluard for the TEM observations.

References

[1] B.L. Risteska Stojkoska, K. V. Trivodaliev, A review of Internet of Things for smart home: Challenges and solutions, J. Clean. Prod., 140 (2017) 1454–1464.

[2] C. Lethien, J. Le Bideau, T. Brousse, Challenges and prospects of 3D micro-supercapacitors for powering the Internet of Things, Energy Environ. Sci., (2018).

[3] Y. Liu, Y. Shi, X. Xu, Evolution and application of all-in-one electrochemical energy storage system, Energy Storage Mater., 41 (2021) 677–696.

[4] J.R. Miller, Valuing reversible energy storage, Science, 335 (2012) 1312–1313.

[5] P. Simon, Y. Gogotsi, Materials for electrochemical capacitors, Nat. Mater., 7 (2008) 845–854.

[6] M.M. Shaijumon, E. Perre, B. Daffos, P.L. Taberna, J.M. Tarascon, P. Simon, Nanoarchitectured 3D cathodes for Li-ion microbatteries, Adv. Mater., 22 (2010) 4978–4981.

[7] J.H. Pikul, J. Liu, P. V. Braun, W.P. King, Integration of high capacity materials into interdigitated mesostructured electrodes for high energy and high power density primary microbatteries, J. Power Sources, 315 (2016) 308–315.

[8] M. Nasreldin, R. Delattre, C. Calmes, M. Ramuz, V.A. Sugiawati, S. Maria, J.L. de B. de la Tocnaye, T. Djenizian, High performance stretchable Li-ion microbattery, Energy Storage Mater., 33 (2020) 108–115.

[9] W. Li, T.L. Christiansen, C. Li, Y. Zhou, H. Fei, A. Mamakhel, B.B. Iversen, J.J. Watkins, High-power lithium-ion microbatteries from imprinted 3D electrodes of sub-10 nm LiMn2O4/Li4Ti5O12 nanocrystals and a copolymer gel electrolyte, Nano Energy, 52 (2018) 431–440.

[10] M. Fehse, R. Trócoli, E. Ventosa, E. Hernández, A. Sepúlveda, A. Morata, A. Tarancón, Ultrafast Dischargeable LiMn2O4 Thin-Film Electrodes with Pseudocapacitive Properties for Microbatteries, ACS Appl. Mater. Interfaces, 9 (2017) 5295–5301.

[11] S. Zheng, H. Huang, Y. Dong, S. Wang, F. Zhou, J. Qin, C. Sun, Y. Yu, Z.S. Wu, X. Bao, Ionogel-based sodium ion micro-batteries with a 3D Na-ion diffusion mechanism

enable ultrahigh rate capability, Energy Environ. Sci., 13 (2020) 821–829.

[12] X. Wang, H. Huang, F. Zhou, P. Das, P. Wen, S. Zheng, P. Lu, Y. Yu, Z.S. Wu, High-voltage aqueous planar symmetric sodium ion micro-batteries with superior performance at low-temperature of −40 ºC, Nano Energy, 82 (2021).

[13] Y. Han, C. Dai, J. Lin, F. Liu, H. Ma, Y. Wang, B. Lu, C. Shao, Q. Guo, X. Jin, X. Zhang, Z. Zhang, A compact aqueous K-ion Micro-battery by a Self-shrinkage assembly strategy, Chem. Eng. J., 429 (2022) 132291.

[14] M. Zhu, J. Hu, Q. Lu, H. Dong, D.D. Karnaushenko, C. Becker, D. Karnaushenko, Y. Li, H. Tang, Z. Qu, J. Ge, O.G. Schmidt, A Patternable and In Situ Formed Polymeric Zinc Blanket for a Reversible Zinc Anode in a Skin-Mountable Microbattery, Adv. Mater., 33 (2021).

[15] Y. Wang, H. Jiang, R. Zheng, J. Pan, J. Niu, X. Zou, C. Jia, A flexible, electrochromic, rechargeable Zn-ion battery based on actiniae-like self-doped polyaniline cathode, J. Mater. Chem. A, 8 (2020) 12799–12809.

[16] Q. Liu, G. Zhang, N. Chen, X. Feng, C. Wang, J. Wang, X. Jin, L. Qu, The First Flexible Dual-Ion Microbattery Demonstrates Superior Capacity and Ultrahigh Energy Density: Small and Powerful, Adv. Funct. Mater., 30 (2020) 1–10.

[17] S. Zhai, N. Wang, X. Tan, K. Jiang, Z. Quan, Y. Li, Z. Li, Interface-Engineered Dendrite-Free Anode and Ultraconductive Cathode for Durable and High-Rate Fiber Zn Dual-Ion Microbattery, Adv. Funct. Mater., 31 (2021).

[18] J.I. Hur, L.C. Smith, B. Dunn, High Areal Energy Density 3D Lithium-Ion Microbatteries, Joule, 2 (2018) 1187–1201.

[19] M. Chan, D. Estève, J.-Y. Fourniols, C. Escriba, E. Campo, Smart wearable systems: Current status and future challenges, Artif Intell Med, 56 (2012) 137–156.

[20] M. Wang, W. Yao, P. Zou, S. Hu, H. Zhu, K. Liu, C. Yang, Battery-on-Separator: A platform technology for arbitrary-shaped lithium ion batteries for high energy density storage, J. Power Sources, 490 (2021).

[21] S. Zheng, Z.S. Wu, F. Zhou, X. Wang, J. Ma, C. Liu, Y.B. He, X. Bao, All-solid-state planar integrated lithium ion micro-batteries with extraordinary flexibility and high-temperature performance, Nano Energy, 51 (2018) 613–620.

[22] Y. Zhang, L. Wang, Z. Guo, Y. Xu, Y. Wang, H. Peng, High-Performance Lithium-Air Battery with a Coaxial-Fiber Architecture, Angew. Chemie - Int. Ed., 55 (2016) 4487–4491.

[23] S. Kang, S.Y. Hong, N. Kim, J. Oh, M. Park, K.Y. Chung, S.S. Lee, J. Lee, J.G. Son, Stretchable Lithium-Ion Battery Based on Re-entrant Micro-honeycomb Electrodes and Cross-Linked Gel Electrolyte, ACS Appl. Mater. Interfaces, (2020).

[24] S.W. Song, K.C. Lee, H.Y. Park, High-performance flexible all-solid-state microbatteries based on solid electrolyte of lithium boron oxynitride, J. Power Sources, 328 (2016) 311–317.

[25] C. (John) Zhang, L. McKeon, M.P. Kremer, S.H. Park, O. Ronan, A. Seral-Ascaso, S. Barwich, C. Coileáin, N. McEvoy, H.C. Nerl, B. Anasori, J.N. Coleman, Y. Gogotsi, V. Nicolosi, Additive-free MXene inks and direct printing of micro-supercapacitors, Nat. Commun., 10 (2019) 1–9.

[26] X. Li, H. Li, X. Fan, X. Shi, J. Liang, 3D-Printed Stretchable Micro-Supercapacitor with Remarkable Areal Performance, Adv. Energy Mater., 10 (2020) 1–12.

[27] X. Wang, S. Zheng, F. Zhou, J. Qin, X. Shi, S. Wang, C. Sun, X. Bao, Z.S. Wu, Scalable fabrication of printed Zn//MnO2 planar micro-batteries with high volumetric energy density and exceptional safety, Natl. Sci. Rev., 7 (2020) 64–72.

[28] C.B. Arnold, R.C. Wartena, K.E. Swider-Lyons, A. Pique, Direct-write planar microultracapacitors by laser engineering, J. Electrochem. Soc., 150 (2003) A571.

[29] M.F. El-Kady, V. Strong, S. Dubin, R.B. Kaner, Laser scribing of high-performance and flexible graphene-based electrochemical capacitors, Science, 335 (2012) 1326–1330.

[30] Rahul Mukherjee, Abhay Varghese Thomas, Ajay Krishnamurthy, Nikhil Koratkar, Photothermally Reduced graphene as high-power anodes for lithium-ion batteries, ACS Nano, 6 (2012) 7867–7878.

[31] W. Pfleging, A review of laser electrode processing for development and manufacturing of lithium-ion batteries, Nanophotonics, 7 (2018) 549–573.

[32] Y. Zhang, S. Zheng, F. Zhou, X. Shi, C. Dong, P. Das, J. Ma, K. Wang, Z.S. Wu, Multi-Layer Printable Lithium Ion Micro-Batteries with Remarkable Areal Energy Density and Flexibility for Wearable Smart Electronics, Small, 2104506 (2021) 1–8.

[33] E. Alhajji, F. Zhang, H.N. Alshareef, Status and Prospects of Laser-Induced Graphene for Battery Applications, Energy Technol., 9 (2021) 1–15.

[34] N. Kurra, B. Ahmed, Y. Gogotsi, H.N. Alshareef, MXene-on-paper coplanar microsupercapacitors, Adv. Energy Mater., 6 (2016) 1–8.

[35] J. Shi, S. Wang, X. Chen, Z. Chen, X. Du, T. Ni, Q. Wang, L. Ruan, W. Zeng, Z. Huang, An Ultrahigh Energy Density Quasi-Solid-State Zinc Ion Microbattery with Excellent Flexibility and Thermostability, Adv. Energy Mater., 9 (2019) 1–9.

[36] W. Lai, Y. Wang, Z. Lei, R. Wang, Z. Lin, C.P. Wong, F. Kang, C. Yang, High performance, environmentally benign and integratable Zn//MnO2 microbatteries, J. Mater. Chem. A, 6 (2018) 3933–3940.

[37] M. Nasreldin, R. Delattre, M. Ramuz, C. Lahuec, T. Djenizian, J.L. de B. de la Tocnaye, Flexible Micro-battery for powering smart contact lens, Sensors, 19 (2019) 2062.

[38] J.Y. Hwang, M.F. El-Kady, Y. Wang, L. Wang, Y. Shao, K. Marsh, J.M. Ko, R.B. Kaner, Direct preparation and processing of graphene/RuO2 nanocomposite electrodes for high-performance capacitive energy storage, Nano Energy, 18 (2015) 57–70.

[39] K. Brousse, S. Nguyen, A. Gillet, S. Pinaud, R. Tan, A. Meffre, K. Soulantica, B. Chaudret, P.L. Taberna, M. Respaud, P. Simon, Laser-scribed Ru organometallic complex for the preparation of RuO2 micro-supercapacitor electrodes on flexible substrate, Electrochim. Acta, 281 (2018) 816–821.

[40] K. Brousse, S. Pinaud, S. Nguyen, P.F. Fazzini, R. Makarem, C. Josse, Y. Thimont, B. Chaudret, P.L. Taberna, M. Respaud, P. Simon, Facile and Scalable Preparation of Ruthenium Oxide-Based Flexible Micro-Supercapacitors, Adv. Energy Mater., 10 (2020) 1903136.

[41] C. Arico, S. Ouendi, P.L. Taberna, P. Roussel, P. Simon, C. Lethien, Fast Electrochemical Storage Process in Sputtered Nb2O5 Porous Thin Films, ACS Nano, 13 (2019) 5826–5832.

[42] J. Come, V. Augustyn, J.W. Kim, P. Rozier, P.-L. Taberna, P. Gogotsi, J.W. Long, B. Dunn, P. Simon, Electrochemical kinetics of nanostructured Nb2O5 electrodes, J.

Electrochem. Soc., 161 (2014) A718–A725.

[43] T. Brousse, D. Belanger, J.W. Long, To be or not to be pseudocapacitive?, J. Electrochem. Soc., 162 (2015) A5185–A5189.

[44] S. Ouendi, C. Arico, F. Blanchard, J.-L. Codron, X. Wallart, P.L. Taberna, P. Roussel, L. Clavier, P. Simon, C. Lethien, Synthesis of T-Nb2O5 thin-films deposited by Atomic Layer Deposition for miniaturized electrochemical energy storage devices, Energy Storage Mater., 16 (2019) 581–588.

[45] M. Mohammadifar, A. Massoudi, N. Naderi, M.J. Eshraghi, Fabrication of Nb 2 O 5 Nanosheets for Lithium-ion Micro-batteries, Adv. Ceram. Prog., 7 (2021) 1–9.

[46] G. Liu, B. Jin, K. Bao, H. Xie, J. Guo, X. Ji, R. Zhang, Q. Jiang, Facile synthesis of porous Nb2O5 microspheres as anodes for lithium-ion batteries, Int. J. Hydrogen Energy, 42 (2017) 6065–6071.

[47] S. Ramakrishna, A. Le Viet, M. V. Reddy, R. Jose, B.V.R. Chowdari, Nanostructured Nb2O5 polymorphs by electrospinning for rechargeable lithium batteries, J. Phys. Chem. C, 114 (2010) 664–671.

[48] V. Augustyn, J. Come, M.A. Lowe, J.W. Kim, P.L. Taberna, S.H. Tolbert, H.D. Abruña, P. Simon, B. Dunn, High-rate electrochemical energy storage through Li + intercalation pseudocapacitance, Nat. Mater., 12 (2013) 518–522.

[49] J. Come, P.-L. Taberna, S. Hamelet, C. Masquelier, P. Simon, Electrochemical Kinetic Study of LiFePO4 Using Cavity Microelectrode, J. Electrochem. Soc., 158 (2011) A1090.

[50] M. Hallot, P. Roussel, C. Lethien, Sputtered LiNi 0.5 Mn 1.5 O 4 Thin Films for Lithium-Ion Microbatteries , ACS Appl. Energy Mater., (2021).

[51] G.D. Salian, C. Lebouin, A. Demoulin, M.S. Lepihin, S. Maria, A.K. Galeyeva, A.P. Kurbatov, T. Djenizian, Electrodeposition of polymer electrolyte in nanostructured electrodes for enhanced electrochemical performance of thin-film Li-ion microbatteries, J. Power Sources, 340 (2017) 242–246.